CONDENSED MATTER PHYSICS

Yu-Shiba-Rusinov bands in ferromagnetic superconducting diamond

Gufei Zhang[1]*†, Tomas Samuely[2]*†, Naoya Iwahara[3,4]*†, Jozef Kačmarčík[2], Changan Wang[5], Paul W. May[6], Johanna K. Jochum[7,8], Oleksandr Onufriienko[2], Pavol Szabó[2], Shengqiang Zhou[5], Peter Samuely[2], Victor V. Moshchalkov[9], Liviu F. Chibotaru[3]*, Horst-Günter Rubahn[1]

The combination of different exotic properties in materials paves the way for the emergence of their new potential applications. An example is the recently found coexistence of the mutually antagonistic ferromagnetism and superconductivity in hydrogenated boron-doped diamond, which promises to be an attractive system with which to explore unconventional physics. Here, we show the emergence of Yu-Shiba-Rusinov (YSR) bands with a spatial extent of tens of nanometers in ferromagnetic superconducting diamond using scanning tunneling spectroscopy. We demonstrate theoretically how a two-dimensional (2D) spin lattice at the surface of a three-dimensional (3D) superconductor gives rise to the YSR bands and how their density-of-states profile correlates with the spin lattice structure. The established strategy to realize new forms of the coexistence of ferromagnetism and superconductivity opens a way to engineer the unusual electronic states and also to design better-performing superconducting devices.

INTRODUCTION

The interplay between different coexisting physical properties induces emergent phenomena, opening a way to design new electronic devices. The investigated mutual interactions between electrical conductivity/superconductivity and magnetism give rise to, for example, colossal magnetoresistance in manganese oxides (*1*) and superconducting pairing by spin fluctuation in iron pnictides. These mutual interactions are also at the heart of Majorana bound states, which arise from the interaction of chiral magnetic fields with a superconducting condensate and are natural candidates for topologically protected qubits (*2*–*5*). In this context, a new intriguing case where superconductivity and ferromagnetism coexist was recently found in hydrogenated boron-doped diamond films (*6*).

To assess the effect of magnetic perturbation on superconductivity, one powerful approach is the analysis of the influence of individual magnetic impurities or groups of impurities on the superconducting state. Their effect has been extensively revealed in various superconductors (*7*), where it was found that individual local magnetic moments interacting with superconducting electrons give rise to in-gap localized states, called Yu-Shiba-Rusinov (YSR) states (*8*–*10*). For the investigation of such localized YSR states, scanning tunneling microscopy/spectroscopy (STM/S) is a methodology of choice, because it directly provides the in-gap local density of states (DOS) with high spatial and energy resolution (*7*, *11*–*16*).

Here, we performed STM/S measurements on ferromagnetic superconducting diamond. In contrast to conventional YSR states localized within few nanometers, we find YSR states with a spatial extent of tens of nanometers, indicating strong delocalization of the electronic excitations. We model the hydrogenated boron-doped diamond as a three-dimensional (3D) superconductor with a 2D spin lattice at the surface. To reproduce the STM/S results within the Bogoliubov-de Gennes (BdG) theory, we assume that hydrogen atoms adsorbed at the surface of boron-doped diamond nanocrystallites arrange in islands of ordered 2D lattices, giving rise to correspondingly ordered islands of magnetic impurities. The resulting impurity states correspond to YSR bands, whose properties strongly depend on the structure of the underlying lattice of localized spins. Hence, systems such as hydrogenated boron-doped diamond are good platforms for hosting such YSR bands.

RESULTS

Hydrogenated boron-doped diamond

Heavily boron-doped polycrystalline chemical vapor deposited diamond films with a hydrogen-terminated surface were used for this research. Structural and compositional analyses indicate that the polycrystalline diamond films are metal free (*6*) and have a thickness of ~900 nm, a mean grain size of ~800 nm, and a boron concentration of ~1.5×10^{21} cm^{-3}. Raman spectroscopy confirms that the sample surface is hydrogen-terminated (*6*).

Coexistent superconductivity and ferromagnetism

The onset of the superconducting state ($\rho = 0$) takes place at 2.7 K in the hydrogenated boron-doped diamond. To gain insight into the dimensionality of the system, we measured the resistive superconducting transition $\rho(T)$ in different magnetic fields, $\mu_0 H$, which were applied perpendicular and parallel to the sample (see Fig. 1, A and B). In contrast to the linear dependences of the offset temperature of the resistive superconducting transition on the applied magnetic fields, the $\mu_0 H_{C2}$-T phase boundaries, as determined by the onset temperature of the resistive superconducting transition, are in good agreement with quadratic fits (see Fig. 1C). Because of the quantum

[1]NanoSYD, Mads Clausen Institute and DIAS Danish Institute for Advanced Study, University of Southern Denmark, Alsion 2, DK-6400 Sonderborg, Denmark. [2]Centre of Low Temperature Physics, Institute of Experimental Physics, Slovak Academy of Sciences & Faculty of Science, P. J. Safarik University, Kosice, Slovakia. [3]Theory of Nanomaterials Group, KU Leuven, Celestijnenlaan 200F, B-3001 Heverlee, Belgium. [4]Department of Chemistry, National University of Singapore, Block S8 Level 3, 3 Science Drive 3, Singapore 117543, Singapore. [5]Helmholtz-Zentrum Dresden-Rossendorf, Institute of Ion Beam Physics and Materials Research, Bautzner Landstr. 400, 01328 Dresden, Germany. [6]School of Chemistry, University of Bristol, Bristol BS8 1TS, UK. [7]Laboratory of Solid State Physics and Magnetism, KU Leuven, B-3001 Heverlee, Belgium. [8]Heinz Maier-Leibnitz Zentrum (MLZ), Technische Universität München, Lichtenbergstrasse 1, 85748 Garching, Germany. [9]Institute for Nanoscale Physics and Chemistry, KU Leuven, 3001 Heverlee, Belgium.
*Corresponding author. Email: gufei@mci.sdu.dk (G.Z.); tomas.samuely@upjs.sk (T.S.); naoya.iwahara@gmail.com (N.I.); liviu.chibotaru@kuleuven.be (L.F.C.)
†These authors contributed equally to this work.

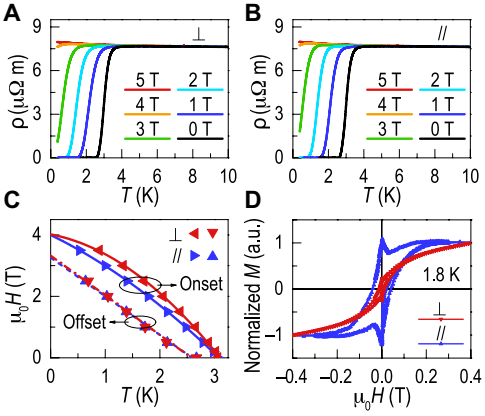

Fig. 1. Coexistent superconductivity and ferromagnetism in hydrogenated boron-doped diamond. Resistive superconducting transitions in (**A**) perpendicular (⊥) and (**B**) parallel (//) applied magnetic fields, respectively. (**C**) The temperature dependences of the critical field, $\mu_0 H(T)$, measured in magnetic fields perpendicular and parallel to the sample. To build up the $\mu_0 H$-T phase boundaries, a criterion was set at 95% of the normal-state resistivity to determine the onset critical temperature, and the resistive superconducting transition was linearly extrapolated down to $\rho = 0$ for the determination of the offset critical temperature in different magnetic fields. The $\mu_0 H$-T phase boundaries are extrapolated to zero temperature by quadratic fits (solid curves) and linear fits (dashed lines), respectively. (**D**) Magnetization hysteresis loops measured at 1.8 K in magnetic fields perpendicular and parallel to the sample. The magnetization, M, is normalized to its value at 0.4 T. a.u., arbitrary units.

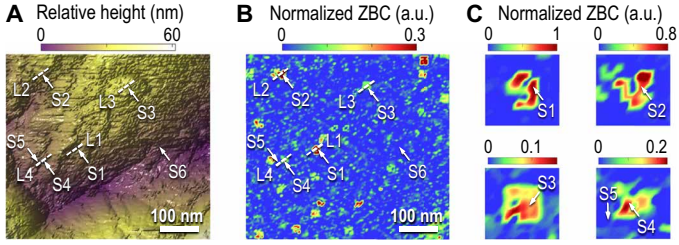

Fig. 2. Topography and spectroscopic mapping of zero-bias conductance in hydrogenated boron-doped diamond. (**A**) Topography of the diamond surface. Arrows (S1 to S6) indicate the location of the characteristic YSR bands as shown in Figs. 3A and 4A, and dashes (L1 to L4) indicate the direction of the spectroscopic mapping in Fig. 3A. (**B**) Zero-bias conductance map acquired at 0.5 K, well below the superconducting transition temperature. The map was constructed by normalizing the tunneling spectra to the dI/dV value at 5 mV, far outside the superconducting gap, and measuring the zero-bias conductance. The arrows and dashes indicate the same locations in (A), respectively. (**C**) Magnifications (39 nm × 39 nm) of the "puddles" where the characteristic YSR bands in Figs. 3 and 4 are observed.

confinement of the superconducting order parameter in the presence of out-of-plane grain boundaries and twin boundaries, the $\mu_0 H_{C2}$-T phase boundary measured in perpendicular fields overshoots the in-plane phase boundary at finite temperatures, revealing a crystallite geometry-induced anomalous superconducting anisotropy in the diamond films. When extrapolating the $\mu_0 H_{C2}$-T phase boundaries down to zero temperature, the quadratic fits converge at $\mu_0 H_{C2}(0\ \mathrm{K}) \sim 4$ T (see Fig. 1C). According to $\xi_{GL} = [\Phi_0/2\pi\ \mu_0 H_{C2}(0\ \mathrm{K})]^{0.5}$ with Φ_0 being the flux quantum, the Ginzburg-Landau coherence length ξ_{GL} is determined to be 9.1 nm. Despite the superconducting anisotropy at finite temperatures, the substantial distinction between ξ_{GL} and film thickness indicates the 3D nature of the superconductivity.

The magnetization hysteresis loops measured below the superconducting transition temperature show characteristics of both superconductivity and ferromagnetism (see Fig. 1D). The former is featured with the central peak and the low-field diamagnetism in the virgin curve, while the latter is reflected in the overall shape of the loops. The temperature-induced evolution of such anomalous hysteresis loops has been reported in (*6*). The presence of ferromagnetism in various forms of metal-free carbon has remained an intriguing question for decades. Although both sp^2/sp^3 defects and hydrogenation have been commonly used to explain the ferromagnetism observed in different forms of carbon (*6*), polycrystalline diamond rich in sp^2/sp^3 defects but without hydrogenation did not show any ferromagnetic behavior (*17*). Furthermore, theoretical calculations demonstrated that unhydrogenated carbon sites and hydrogen impurities can give rise to local magnetic moments in graphene and diamond, respectively (*18*–*20*).

The substantial distinction between the in-plane and out-of-plane magnetization loops indicates the in-plane easy axis of magnetization (see Fig. 1D). Taking into account the robust 3D nature of the superconductivity, the diamond films cannot be simply treated as conventional ferromagnets in the form of thin film, where similar magnetic anisotropy is mainly caused by shape anisotropy (*21*). The anomalous superconducting anisotropy mentioned above cannot be a cause of the magnetic anisotropy, either, because at 1.8 K and in the magnetic field range of 0 to 0.4 T, the diamond films demonstrate no superconducting anisotropy (see Fig. 1C). Accordingly, the observed magnetic anisotropy is highly likely due to the anisotropic distribution of magnetic impurities.

YSR bands observed in direct local measurements

As revealed by STM/S measurements performed at 0.5 K on the surface of the hydrogenated boron-doped diamond (see Fig. 2A), the zero-bias tunneling conductance map demonstrates strong modulations of the local DOS on the nanoscale, which appear as "puddles" (see Fig. 2, B and C). The tunneling conductance spectra acquired over the puddles show symmetric maxima and minima around the zero energy inside the superconducting gap 2Δ (see Fig. 3A), which are fingerprints of the YSR effect. In contrast to the localized YSR states that are restricted to a few atomic distances in 3D systems (*14*), these collective excitations extend up to tens of nanometers, revealing the delocalization of the YSR states and the emergence of YSR bands. The extraordinarily large spatial extension of our observed YSR bands can also be seen in the spatial dependence of the integrated in-gap DOS (see Fig. 3B).

The observed YSR bands demonstrate a variety of DOS profiles (see Figs. 3A and 4, A and B). Apart from the pair of peaks at finite energies ($E_{YSR} \sim \pm 0.39\Delta$), the tunneling spectra S1 and S4 both show a third peak at zero energy inside the superconducting gap $2\Delta \sim 3$ meV. Along with the peaks at $E_{YSR} \sim \pm 0.22\Delta$ in spectrum S2, a pair of kinks ($E_{YSR} \sim \pm 0.39\Delta$) emerge at the shoulders of the peaks. Spectrum S3 exhibits two peaks at $E_{YSR} \sim \pm 0.35\Delta$ and two kinks at $E_{YSR} \sim \pm 0.21\Delta$, while spectrum S5 reveals the emergence of two pairs of peaks at $E_{YSR} \sim \pm 0.61\Delta$ and $E_{YSR} \sim \pm 0.2\Delta$, respectively. Note that among these YSR bands, even S5 shows a spatial extent of ~9 nm (see L4 in Fig. 3A). In contrast to these YSR bands, the tunneling spectra outside the puddles exhibit Bardeen-Cooper-Schrieffer–like gap structures (see spectrum S6 in Fig. 4, A and B).

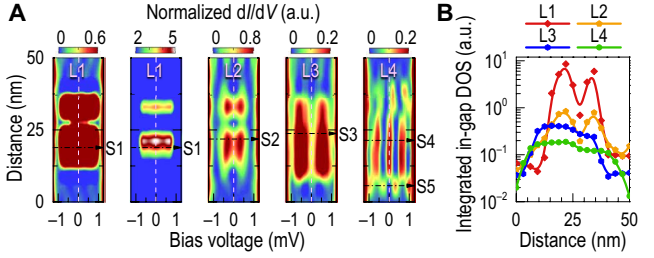

Fig. 3. YSR bands in hydrogenated boron-doped diamond. (**A**) Spatial and energy evolutions of the tunneling conductance, d*I*/d*V*, along the dashes in Fig. 2. The tunneling conductance along L1 is shown in two panels with different color scales for the clarity of both spatial and energy evolutions. Dash-dotted arrows (S1 to S5) indicate the location of the characteristic YSR bands as shown in Fig. 4A. (**B**) Spatial evolution of the integrated in-gap DOS. The integration was performed over the range from −1 to +1 mV. The solid curves are a guide to the eye.

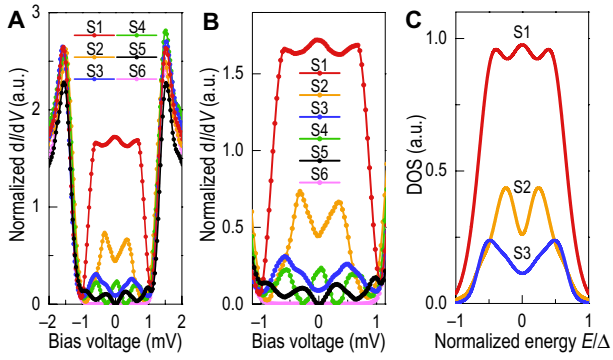

Fig. 4. Comparison between measured and calculated YSR bands. (**A**) Characteristic experimental spectra acquired at S1 to S6 in Fig. 2. The tunneling spectra are normalized to the conductance at 5 mV. (**B**) Magnification of the measured in-gap DOS. (**C**) YSR bands calculated using the tight-binding BdG equation in correspondence to the measured tunneling conductance spectra S1 to S3.

Theoretical modeling of YSR bands with a tight-binding BdG approach

To give insights into the origin of the various DOS profiles (see Fig. 4, A and B), we developed a microscopic theory. The ferromagnetism can arise from both bulk hydrogen impurities (*20*, *22*, *23*) and hydrogen islands at the surface, and the mechanism is still largely unknown. Because we observed extended but finite (several tens of nanometers) regions with nonnegligible in-gap DOS, we speculate that its origin is the presence of islands of magnetic impurities located at or close to the surface, which interact with the bulk superconducting state. Moreover, although the present STM/S measurements do not have atomic resolution and the character of the distribution of the impurities cannot be determined (see Materials and Methods), it should have strong correlation with the type of the surface. The surface of the polycrystalline nanodiamond films is far from flat, and there are (111) and (100) surfaces (*6*), giving rise to triangular and rectangular spin lattices on them, respectively (see Fig. 5). Given the strong exchange interaction between the magnetic centers (with Curie temperature >400 K), the spins on the surface can be treated as classical ones.

The electronic bands in the presence of a spin lattice were calculated with a tight-binding BdG approach with the localized YSR states on spin sites as the basis (*4*, *5*). The BdG equation in the presence of the classical spin S at $\mathbf{R}_j$ is given by

$$\begin{pmatrix} \xi_k & \Delta \\ \Delta & -\xi_k \end{pmatrix} \mathbf{w_k} - \sum_j J S \begin{pmatrix} 1 & 0 \\ 0 & 1 \end{pmatrix} e^{-i\mathbf{k}\cdot\mathbf{R}_j} \mathbf{w}(\mathbf{R}_j) = E\,\mathbf{w_k}$$

where $\mathbf{w_k}$ stands for the quasi-particle states characterized by wave vector $\mathbf{k}$, $\mathbf{w}(\mathbf{R}_j)$ indicates the localized YSR state at site j, E is energy, ξ_k is the free electron energy with respect to chemical potential, J is the exchange coupling parameter, $S = 1/2$ is the spin, and Δ is the superconducting order parameter. We transformed this equation into the tight-binding form on the basis of localized YSR states and then calculated the quasi-particle bands (see Materials and Methods). To reproduce the experimental DOS, we treated the dimensionless exchange interaction $\alpha = \pi\nu_0 JS$ between the spins and conduction electrons (ν_0 is the DOS of the electronic band at the Fermi energy) and the distance between the spin sites as variables.

Among the experimentally obtained DOS, we focused on S1, S2, and S3, which clearly show the band nature (Fig. 3A). Figure 4C shows the theoretical DOS calculated using rectangular lattices for S1 and S2 and a triangular lattice for S3 with $\alpha = 0.7$ (see Materials and Methods for other parameters). The dimensions of the rectangles are 9×10 and 9×13 for S1 and S2, respectively, and the length of the side of the equilateral triangle is 12 for S3, all in units of diamond lattice constant, $a = 3.57$ Å. The numbers and the positions of the maxima of the DOS within the superconducting gap are in good agreement with the experimental data. Qualitatively different DOS profiles were obtained for S1 and S2 using the same spin lattice structure and α, because the interaction between the YSR states oscillates with respect to the distance. The good agreement between the theoretical modeling and the experimental data confirms that the observed in-gap excitations are YSR bands. Moreover, the diameter of the YSR localized state (*14*) and the distance between the nearest lattice points are comparable to each other, which is consistent with the absence of the spatial variation of the DOS in our experimental spectra S1 to S3 obtained with the present spatial resolution of STM/S (see Fig. 3A). Despite the fact that the magnetic impurities tend to destroy the superconductivity, the superconducting temperature of the ferromagnetic diamond is almost unchanged, compared to other doped diamond superconductors (*24*, *25*). This is explained by the low concentration of the hydrogen-related magnetic impurities on surface as readily understood from the dimensions of the lattices used for the calculations. The theoretical analysis also suggests that the present system is close to the regime of gapless superconductivity due to the classical spins (*9*).

DISCUSSION

In summary, we unveiled the presence of long-range coherent YSR bands in a 3D ferromagnetic superconductor, heavily boron-doped diamond with hydrogen-terminated surface. In contrast to localized YSR states, the observed YSR bands show a spatial extent up to tens of nanometers. Limited by the resolution of STM/S measurements on polycrystalline diamond, the spatial distribution of magnetic impurities cannot be extracted from our experiments. By developing a microscopic theory for a 3D superconductor with a 2D spin lattice at its surface, we reproduced the experimental DOS profiles of the observed YSR bands in ferromagnetic superconducting diamond reasonably well. Apart from the Fulde-Ferrell-Larkin-Ovchinnikov state (*26*, *27*) and the so-called domain wall superconductivity (*28*, *29*), introduction of the sparse magnetic impurity lattice is another form

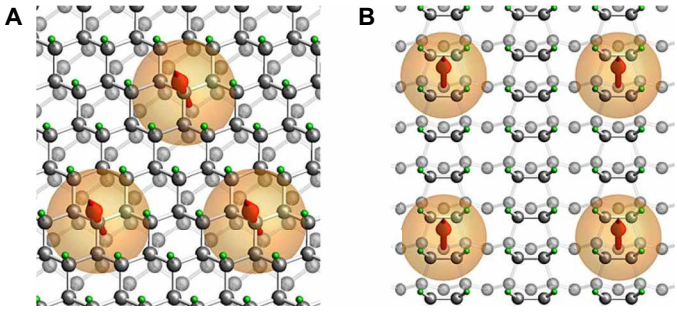

Fig. 5. Arrangements of impurity spins at the diamond surface for tight-binding calculations of YSR bands. (**A**) Triangular spin lattice for the (111) surface. (**B**) Rectangular spin lattice for the (100) surface. Green and black pellets represent the surface hydrogen and carbon atoms, respectively. Red arrows and orange spheres denote the impurity spins and localized YSR states, respectively. The hybridization of the localized YSR states gives rise to the emergence of YSR bands.

of the coexistence of the two mutually antagonistic orderings, ferromagnetism and superconductivity. The present results suggest the possibility to construct hybrid systems consisting of, e.g., sparse 2D ferromagnetic lattice and superconductor with spin-orbit coupling (*5*) to realize unconventional topological superconducting phases.

MATERIALS AND METHODS

Sample preparation

The heavily boron-doped and hydrogenated polycrystalline diamond films were grown using hot filament chemical vapor deposition (CVD). The substrates were undoped single-crystal Si (100) with a 30-nm-thick layer of SiO_2 on the surface. The wafers were seeded with a colloidal suspension of diamond nanoparticles (diameter ~20 nm) using an electrospray process (seeding density ~3×10^{10} cm^{-2}) (*30*). The seeded substrate was then placed 3 mm below a 2200°C tantalum filament in the CVD reactor. A gas mixture of 0.6% CH_4 in H_2 (total flow, 200 standard cubic centimeters per minute) was thermally dissociated using the hot filament for diamond growth onto the substrate, which was maintained at 800°C. Boron doping was realized by adding diborane (B_2H_6) to the gas mixture with a B_2H_6/CH_4 ratio of 5%. To ensure that the diamond surface was hydrogen-terminated, after deposition was complete, the CH_4 and B_2H_6 flows were switched off, while the sample remained under the filaments for 1 min in pure hydrogen gas. The filaments were then switched off, allowing the sample to cool back to room temperature under flowing H_2 in ~30 min (*6*).

Electrical transport and magnetization measurements

The electrical transport properties and magnetization of the samples were measured using a Heliox ^{3}He cryostat and an MPMS3 system, respectively.

Scanning tunneling microscopy/spectroscopy

The differential tunneling conductance spectra were acquired by means of a homemade STM (*31*) cooled to 0.5 K by a commercial Janis SSV cryomagnetic system with a ^{3}He refrigerator. The atomically sharp gold STM tip was obtained in situ by systematically impaling the tip into a clean gold surface. To measure the tunneling current spectra, the feedback loop was turned off, and the tunneling current at different bias voltages applied to the tip was recorded. The applied bias voltage was swept from −10 to +10 mV with an interval of ~20 μV, which is smaller than the width of the in-gap peaks by one order of magnitude. The initial tunneling resistance was 5 megohms. Because the gold tip features a constant DOS, the differential conductance derived numerically from the current spectra represents the local DOS of the diamond surface. Despite the atomic sharpness of the STM tip, the spatial resolution of our STM/S measurements was limited to ~3 nm because of the surface roughness of the lab-grown polycrystalline diamond films. As a result of the newly formed nucleation sites, the surface of the diamond crystallites is corrugated on the nanoscale and far from flat. The nanoscale corrugations give rise to additional noise, which limits the spatial resolution of the STM/S measurements.

Theoretical modeling

The BdG equation was transformed into the tight-binding form on the basis of localized YSR states (*4*).

$$\mathbf{w}(\mathbf{R}_i) = \sum_j -JS \begin{pmatrix} E\,I_0(R_{ij}) + I_1(R_{ij}) & \Delta\, I_0(R_{ij}) \\ \Delta\, I_0(R_{ij}) & E\,I_0(R_{ij}) - I_1(R_{ij}) \end{pmatrix} \mathbf{w}(\mathbf{R}_j) \quad (1)$$

where $R_{ij} = |\mathbf{R}_i - \mathbf{R}_j|$, $I_0(R) = (2\pi)^{-3} \int d^3\mathbf{k}\, e^{i\mathbf{k}\cdot\mathbf{R}}/(E^2 - \xi_{k2} - \Delta^2)$, and $I_1(R) = (2\pi)^{-3} \int d^3\mathbf{k}\ \xi_k e^{i\mathbf{k}\cdot\mathbf{R}} / \left(E^2 - \xi_k^2 - \Delta^2\right)$. These integrals were evaluated under the condition of $(\hbar k_F)^2/2m_e >> \hbar\omega_D >> \Delta > E$ as

$$\begin{aligned} I_0(R) &\simeq -\frac{\pi\nu_0}{\sqrt{\Delta^2 - E^2}} \frac{\sin(k_F R)}{k_F R} \exp\left(-\frac{\sqrt{\Delta^2 - E^2}}{\hbar\upsilon_F} R \right), \\ I_1(R) &\simeq -\frac{\pi\nu_0}{k_F R} \left\{ \left[\exp\left(-\frac{\sqrt{\Delta^2 - E^2}}{\hbar\upsilon_F} R \right) - 1 \right] \cos(k_F R) + \right. \\ &\left. \frac{\sqrt{\Delta^2 - E^2}}{\hbar\upsilon_F k_F} \exp\left(-\frac{\sqrt{\Delta^2 - E^2}}{\hbar\upsilon_F} R \right) \sin(k_F R) \right\} \\ &+ \frac{\pi\nu_0}{k_F R} \frac{2}{\pi} \left[-\cos(k_F R)\, \mathrm{Si}\left(\frac{\omega_D R}{\upsilon_F} \right) - \sin(k_F R) \frac{\sin\left(\frac{\omega_D R}{\upsilon_F}\right)}{k_F R} \right] \end{aligned} \quad (2)$$

where ħ is the reduced Planck constant; k_F and υ_F are the wave vector and velocity at the Fermi energy, respectively; m_e is the mass of electron; ω_D is the Debye frequency; and Si(x) is the sine integral. The electron attraction and Δ are assumed to be finite when $|\xi_k| < \omega_D$. The expression of I_1 was improved so that small distances can be accurately treated in comparison with the previous work based on asymptotic treatment (*4*).

When there is only one impurity, the eigenvalues E of Eq. 1 reduce to (*8*–*10*)

$$E = \pm\Delta \frac{1 - \alpha^2}{1 + \alpha^2}$$

where $\alpha = \pi\nu_0 JS$. The energy levels appear within the superconducting gap.

Assuming the periodicity of the impurity centers, Eq. 1 was Fourier-transformed with the period of impurity centers

$$\lambda_{\mathbf{q}} \mathbf{w}'_{\mathbf{q}} = \begin{pmatrix} \frac{\sqrt{1 - \lambda_{\mathbf{q}}^2}}{\alpha} & -1 \\ -1 & \frac{\sqrt{1 - \lambda_{\mathbf{q}}^2}}{\alpha} \end{pmatrix} \mathbf{w}'_{\mathbf{q}} - \begin{pmatrix} \lambda_{\mathbf{q}} \tilde{I}_{0,\mathbf{q}} + \tilde{I}_{1,\mathbf{q}} & \tilde{I}_{0,\mathbf{q}} \\ \tilde{I}_{0,\mathbf{q}} & \lambda_{\mathbf{q}} \tilde{I}_{0,\mathbf{q}} - \tilde{I}_{1,\mathbf{q}} \end{pmatrix} \mathbf{w}'_{\mathbf{q}} \quad (3)$$

Here, $\mathbf{w}'_{\mathbf{q}} = \sum_j \mathbf{w}(\mathbf{R}_j) \exp(-i\mathbf{q} \cdot \mathbf{R}_j)$ is the Fourier transformation of $\mathbf{w}(\mathbf{R}_i)$, $\lambda_{\mathbf{q}} = E/\Delta, \tilde{I}_{n,\mathbf{q}}(n = 0, 1)$ is defined by

$$\tilde{I}_{n,\mathbf{q}} = \sum_{j(\neq 0)} e^{-i\mathbf{q}\cdot\mathbf{R}_j} \tilde{I}_n(R_j) \tag{4}$$

$\mathbf{R}_0 = 0$, $\tilde{I}_0(R) = I_0(R)/I_0(0)$, and $\tilde{I}_1(R) = I_1(R)/[\Delta I_0(0)]$. Last, by solving the eigenvalue problem (Eq. 3), we obtained a nonlinear equation for each wave vector $\mathbf{q}$

$$\lambda_{\mathbf{q}} = \frac{\sqrt{1-\lambda_{\mathbf{q}}^2}}{\alpha} - \lambda_{\mathbf{q}} \tilde{I}_{0,\mathbf{q}} \pm \sqrt{(1+\tilde{I}_{0,\mathbf{q}})^2 + \tilde{I}^2{}_{1,\mathbf{q}}} \tag{5}$$

Neither spin-orbit coupling nor edge of the lattice is considered in our theory, and hence, the scenario of the emergence of exotic edge states discussed in (*5*) does not apply.

By numerically solving this equation, we obtained the quasiparticle energy band. For the simulations, $k_F \approx 1 \times 10^9$ to 3×10^9 m^{-1} and $\upsilon_F \approx 7$ to 8 eV Å were taken from (*32*), and $a = 3.57$ Å and $\omega_D \approx 160$ meV for diamond were taken from (*33*). With these parameters, $k_F\, a \approx 1$, $\hbar\upsilon_F/a \approx 2$ eV, $\omega_D/(\upsilon_F/a) \approx 0.08$, and $\Delta/(\hbar\upsilon_F k_F) \approx 0.0005$. The shape of the impurity lattice is either a rectangle or regular triangle. The DOS was convoluted with Gaussian function with standard deviation $\sigma/\Delta = 0.14$, 0.10, and 0.09 for S1, S2, and S3, respectively. The height of the DOS, which depends on the distance between the STM tip and the surface (*14*), was rescaled to match the experimental DOS.

REFERENCES AND NOTES

1. Y. Tokura, N. Nagaosa, Orbital physics in transition-metal oxides. *Science* **288**, 462–468 (2000).
2. S. Nadj-Perge, I. K. Drozdov, J. Li, H. Chen, S. Jeon, J. Seo, A. H. MacDonald, B. A. Bernevig, A. Yazdani, Topological matter. Observation of majorana fermions in ferromagnetic atomic chains on a superconductor. *Science* **346**, 602–607 (2014).
3. S. Nadj-Perge, I. K. Drozdov, B. A. Bernevig, A. Yazdani, Proposal for realizing majorana fermions in chains of magnetic atoms on a superconductor. *Phys. Rev. B* **88**, 020407(R) (2013).
4. F. Pientka, L. I. Glazman, F. von Oppen, Topological superconducting phase in helical Shiba chains. *Phys. Rev. B* **88**, 155420 (2013).
5. J. Röntynen, T. Ojanen, Topological superconductivity and high chern numbers in 2D ferromagnetic Shiba lattices. *Phys. Rev. Lett.* **114**, 236803 (2015).
6. G. Zhang, T. Samuely, Z. Xu, J. K. Jochum, A. Volodin, S. Zhou, P. W. May, O. Onufriienko, J. Kačmarčik, J. A. Steele, J. Li, J. Vanacken, J. Vacík, P. Szabó, H. Yuan, M. B. J. Roeffaers, D. Cerbu, P. Samuely, J. Hofkens, V. V. Moshchalkov, Superconducting ferromagnetic nanodiamond. *ACS Nano* **11**, 5358–5366 (2017).
7. A. V. Balatsky, I. Vekhter, J.-X. Zhu, Impurity-induced states in conventional and unconventional superconductors. *Rev. Mod. Phys.* **78**, 373–433 (2006).
8. L. Yu, Bound state in superconductors with paramagnetic impurities. *Acta Phys. Sin.* **21**, 75–91 (1965).
9. H. Shiba, Classical spins in superconductors. *Prog. Theor. Phys.* **40**, 435–451 (1968).
10. A. I. Rusinov, Superconductivity near a paramagnetic impurity. *JETP Lett.* **9**, 85–87 (1969).
11. A. Yazdani, B. A. Jones, C. P. Lutz, M. F. Crommie, D. M. Eigler, Probing the local effects of magnetic impurities on superconductivity. *Science* **275**, 1767–1770 (1997).
12. S.-H. Ji, T. Zhang, Y.-S. Fu, X. Chen, X.-C. Ma, J. Li, W.-H. Duan, J.-F. Jia, Q.-K. Xue, High-resolution scanning tunneling spectroscopy of magnetic impurity induced bound states in the superconducting gap of Pb thin films. *Phys. Rev. Lett.* **100**, 226801 (2008).
13. K. J. Franke, G. Schulze, J. I. Pascual, Competition of superconducting phenomena and Kondo screening at the nanoscale. *Science* **332**, 940–944 (2011).
14. G. C. Ménard, S. Guissart, C. Brun, S. Pons, V. S. Stolyarov, F. Debontridder, M. V. Leclerc, E. Janod, L. Cario, D. Roditchev, P. Simon, T. Cren, Coherent long-range magnetic bound states in a superconductor. *Nat. Phys.* **11**, 1013–1016 (2015).
15. N. Hatter, B. W. Heinrich, M. Ruby, J. I. Pascual, K. J. Franke, Magnetic anisotropy in Shiba bound states across a quantum phase transition. *Nat. Commun.* **6**, 8988 (2015).
16. S. Kezilebieke, M. Dvorak, T. Ojanen, P. Liljeroth, Coupled Yu-Shiba-Rusinov states in molecular dimers on $NbSe_2$. *Nano Lett.* **18**, 2311–2315 (2018).
17. G. Zhang, S. Turner, E. A. Ekimov, J. Vanacken, M. Timmermans, T. Samuely, V. A. Sidorov, S. M. Stishov, Y. Lu, B. Deloof, B. Goderis, G. van Tendeloo, J. van de Vondel, V. V. Moshchalkov, Global and local superconductivity in boron-doped granular diamond. *Adv. Mater.* **26**, 2034–2040 (2014).
18. J. Zhou, Q. Wang, Q. Sun, X. S. Chen, Y. Kawazoe, P. Jena, Ferromagnetism in semihydrogenated graphene sheet. *Nano Lett.* **9**, 3867–3870 (2009).
19. J. L. Lado, J. Fernández-Rossier, Unconventional Yu-Shiba-Rusinov states in hydrogenated graphene. *2D Mater.* **3**, 025001 (2016).
20. K. Kenmochi, K. Sato, A. Yanase, H. Katayama-Yoshida, Materials design of ferromagnetic diamond. *Jpn. J. Appl. Phys.* **44**, L51 (2005).
21. G. Bayreuther, G. Lugert, Magnetization of ultra-thin epitaxial Fe films. *J. Magn. Magn. Mater.* **35**, 50–52 (1983).
22. N. Mizuochi, M. Ogura, H. Watanabe, J. Isoya, H. Okushi, S. Yamasaki, EPR study of hydrogen-related defects in boron-doped p-type CVD homoepitaxial diamond films. *Diamond Relat. Mater.* **13**, 2096–2099 (2004).
23. P. Szirmai, G. Fábián, J. Koltai, B. Náfrádi, L. Forró, T. Pichler, O. A. Williams, S. Mandal, C. Bäuerle, F. Simon, Observation of conduction electron spin resonance in boron-doped diamond. *Phys. Rev. B* **87**, 195132 (2013).
24. Y. Takano, Superconductivity in CVD diamond films. *J. Phys. Condens. Matter* **21**, 253201 (2009).
25. G. Zhang, T. Samuely, H. Du, Z. Xu, L. Liu, O. Onufriienko, P. W. May, J. Vanacken, P. Szabó, J. Kačmarčík, H. Yuan, P. Samuely, R. E. Dunin-Borkowski, J. Hofkens, V. V. Moshchalkov, Bosonic confinement and coherence in disordered nanodiamond arrays. *ACS Nano* **11**, 11746–11754 (2017).
26. P. Fulde, R. A. Ferrell, Superconductivity in a strong spin-exchange field. *Phys. Rev. J. Arch.* **135**, A550–A563 (1964).
27. A. I. Larkin, Y. N. Ovchinnikov, Density of states in inhomogeneous superconductors. *Sov. Phys. JETP* **34**, 1144–1150 (1972).
28. A. I. Buzdin, A. S. Mel'nikov, Domain wall superconductivity in ferromagnetic superconductors. *Phys. Rev. B* **67**, 020503 (2003).
29. M. Iavarone, S. A. Moore, J. Fedor, S. T. Ciocys, G. Karapetrov, J. Pearson, V. Novosad, S. D. Bader, Visualizing domain wall and reverse domain superconductivity. *Nat. Commun.* **5**, 4766 (2014).
30. P. W. May, Diamond thin films: A 21st-century material. *Phil. Trans. R. Soc. A* **358**, 473–495 (2000).
31. T. Samuely, P. Szabó, Z. Pribulová, N. H. Sung, B. K. Cho, T. Klein, V. Cambel, J. G. Rodrigo, P. Samuely, Type II superconductivity in $SrPd_2Ge_2$. *Supercond. Sci. Technol.* **26**, 015010 (2013).
32. T. Yokoya, T. Nakamura, T. Matsushita, T. Muro, Y. Takano, M. Nagao, T. Takenouchi, H. Kawarada, T. Oguchi, Origin of the metallic properties of heavily boron-doped superconducting diamond. *Nature* **438**, 647–650 (2005).
33. N. W. Ashcroft, N. D. Mermin, *Solid State Physics* (Holt, Rinehart and Winston, 1976).

Acknowledgments

Funding: G.Z. thanks the Fabrikant Mads Clausens Fond. T.S., J.K., O.O., P.Sz., and P.Sa. were supported by APVV-18-0358, VEGA 1/0743/19, VEGA 2/0149/16, COST action CA16218 Nanocohybri, and H2020 Infraia 824109 European Microkelvin Platform. N.I. was supported by GOA from KU Leuven and the scientific research grant R-143-000-A80-114 of the National University of Singapore. J.K.J. thanks the Hercules Foundation. **Author contributions:** G.Z. conceived the study and designed the experiments. P.W.M. prepared the samples. T.S., O.O., and P.Sa. performed the scanning tunneling spectroscopy measurements. J.K., G.Z., and P.Sz. measured the electrical transport properties. S.Z., J.K.J., and C.W. carried out the SQUID measurements. G.Z. and T.S. analyzed the data. N.I. and L.F.C. performed the theoretical modeling. G.Z., N.I., and L.F.C. prepared the manuscript with inputs from T.S. and P.W.M. P.Sa., V.V.M., and H.-G.R. took part in the discussions and correction of the manuscript. **Competing interests:** The authors declare that they have no competing interests. **Data and materials availability:** All data needed to evaluate the conclusions in the paper are present in the paper. Additional data related to this paper may be requested from the corresponding authors.

Submitted 24 August 2019
Accepted 3 March 2020
Published 15 May 2020
10.1126/sciadv.aaz2536

Citation: G. Zhang, T. Samuely, N. Iwahara, J. Kačmarčík, C. Wang, P. W. May, J. K. Jochum, O. Onufriienko, P. Szabó, S. Zhou, P. Samuely, V. V. Moshchalkov, L. F. Chibotaru, H.-G. Rubahn, Yu-Shiba-Rusinov bands in ferromagnetic superconducting diamond. *Sci. Adv.* **6**, eaaz2536 (2020).

Yu-Shiba-Rusinov bands in ferromagnetic superconducting diamond

Gufei Zhang, Tomas Samuely, Naoya Iwahara, Jozef Kacmarcík, Changan Wang, Paul W. May, Johanna K. Jochum, Oleksandr Onufriienko, Pavol Szabó, Shengqiang Zhou, Peter Samuely, Victor V. Moshchalkov, Liviu F. Chibotaru and Horst-Günter Rubahn

Sci Adv **6** (20), eaaz2536.
DOI: 10.1126/sciadv.aaz2536